CrossMark

NEID Reveals That the Young Warm Neptune TOI-2076 b Has a Low Obliquity

Robert C. Frazier[1,2], Gudmundur Stefánsson[3,4], Suvrath Mahadevan[1,2,5], Samuel W. Yee[3], Caleb I. Cañas[6], Joshua N. Winn[3], Jacob Luhn[7], Fei Dai[8,9], Lauren Doyle[10,11], Heather Cegla[10,11], Shubham Kanodia[12], Paul Robertson[7], John Wisniewski[13], Chad F. Bender[14], Jiayin Dong[15,31], Arvind F. Gupta[1,2], Samuel Halverson[16], Suzanne Hawley[17], Leslie Hebb[18], Rae Holcomb[7], Adam Kowalski[19,20,21], Jessica Libby-Roberts[1,2], Andrea S. J. Lin[1,2], Michael W. McElwain[22], Joe P. Ninan[23], Cristobal Petrovich[24,25], Arpita Roy[26,27], Christian Schwab[28], Ryan C. Terrien[29], and Jason T. Wright[1,2,30]

[1] Department of Astronomy & Astrophysics, 525 Davey Laboratory, The Pennsylvania State University, University Park, PA, 16802, USA; rcf5201@psu.edu
[2] Center for Exoplanets and Habitable Worlds, 525 Davey Laboratory, The Pennsylvania State University, University Park, PA, 16802, USA
[3] Department of Astrophysical Sciences, Princeton University, 4 Ivy Lane, Princeton, NJ, 08540, USA
[4] NASA Sagan Fellow
[5] ETH Zurich, Institute for Particle Physics & Astrophysics, Switzerland
[6] NASA Goddard Space Flight Center, 8800 Greenbelt Road, Greenbelt, MD, 20771, USA
[7] Department of Physics & Astronomy, The University of California, Irvine, Irvine, CA, 92697, USA
[8] Division of Geological and Planetary Sciences, California Institute of Technology, 1200 E California Blvd, Pasadena, CA, 91125, USA
[9] Department of Astronomy, California Institute of Technology, Pasadena, CA, 91125, USA
[10] Centre for Exoplanets and Habitability, University of Warwick, Coventry, CV4 7AL, UK
[11] Department of Physics, University of Warwick, Coventry, CV4 7AL, UK
[12] Earth and Planets Laboratory, Carnegie Institution for Science, 5241 Broad Branch Road, NW, Washington, DC, 20015, USA
[13] George Mason University, Department of Physics and Astronomy, 4400 University Drive, MS 3F3, Fairfax, VA, 22030, USA
[14] Steward Observatory, The University of Arizona, 933 N. Cherry Ave, Tucson, AZ, 85721, USA
[15] Center for Computational Astrophysics, Flatiron Institute, 162 Fifth Avenue, New York, NY, 10010, USA
[16] Jet Propulsion Laboratory, California Institute of Technology, 4800 Oak Grove Drive, Pasadena, CA, 91109, USA
[17] Astronomy Department, Box 351580, University of Washington, Seattle, WA, 98195, USA
[18] Department of Physics, Hobart and William Smith Colleges, 300 Pulteney Street, Geneva, NY, 14456, USA
[19] Department of Astrophysical and Planetary Sciences, University of Colorado Boulder, 2000 Colorado Ave., Boulder, CO, 80305, USA
[20] National Solar Observatory, University of Colorado Boulder, 3665 Discovery Drive, Boulder, CO, 80303, USA
[21] Laboratory for Atmospheric and Space Physics, University of Colorado Boulder, 3665 Discovery Drive, Boulder, CO, 80303, USA
[22] Exoplanets and Stellar Astrophysics Laboratory, NASA Goddard Space Flight Center, Greenbelt, MD, 20771, USA
[23] Department of Astronomy and Astrophysics, Tata Institute of Fundamental Research, Homi Bhabha Road, Colaba, Mumbai 400005, India
[24] Instituto de Astrofísica, Pontificia Universidad Católica de Chile, Av. Vicuña Mackenna 4860, 782-0436 Macul, Santiago, Chile
[25] Millennium Institute for Astrophysics, Chile
[26] Space Telescope Science Institute, 3700 San Martin Dr, Baltimore, MD, 21218, USA
[27] Department of Physics and Astronomy, Johns Hopkins University, 3400 N Charles St, Baltimore, MD, 21218, USA
[28] School of Mathematical and Physical Sciences, Macquarie University, Balaclava Road, North Ryde, NSW 2109, Australia
[29] Carleton College, One North College St., Northfield, MN, 55057, USA
[30] Penn State Extraterrestrial Intelligence Center, 525 Davey Laboratory, The Pennsylvania State University, University Park, PA, 16802, USA

Abstract

TOI-2076 b is a sub-Neptune-sized planet ($R = 2.39 \pm 0.10\,R_\oplus$) that transits a young ($204 \pm 50\,\mathrm{MYr}$) bright ($V = 9.2$) K-dwarf hosting a system of three transiting planets. Using spectroscopic observations obtained with the NEID spectrograph on the WIYN 3.5 m Telescope, we model the Rossiter–McLaughlin effect of TOI-2076 b, and derive a sky-projected obliquity of $\lambda = -3^{+16\circ}_{-15}$. Using the size of the star ($R = 0.775 \pm 0.015\,R_\odot$), and the stellar rotation period ($P_{\rm rot} = 7.27 \pm 0.23$ days), we estimate an obliquity of $\psi = 18^{+10\circ}_{-9}$ ($\psi < 34°$ at 95% confidence), demonstrating that TOI-2076 b is in a well-aligned orbit. Simultaneous diffuser-assisted photometry from the 3.5 m telescope at Apache Point Observatory rules out flares during the transit. TOI-2076 b joins a small but growing sample of young planets in compact multi-planet systems with well-aligned orbits, and is the fourth planet with an age $\lesssim 300$ Myr in a multi-transiting system with an obliquity measurement. The low obliquity of TOI-2076 b and the presence of transit timing variations in the system suggest the TOI-2076 system likely formed via convergent disk migration in an initially well-aligned disk.

Supporting material: data behind figure

---

[31] Flatiron Research Fellow

---

1. Introduction

Stellar obliquity—the angle between the stellar rotation axis and the planet orbital axis—is a powerful probe of the dynamical formation histories of planetary systems (Albrecht et al. 2022). Stellar obliquities have most successfully been measured with the Rossiter–McLaughlin (RM) effect (McLaughlin 1924; Rossiter 1924), which relies on measuring

spectral line distortions approximated as radial velocity (RV) shifts during as a companion transits the host star. RM measurements made over the last two decades have revealed a broad distribution of sky-projected obliquities, λ, from well-aligned to highly misaligned systems (see Albrecht et al. 2022 and references therein).

However, the RM effect is primarily sensitive to the sky projection of the obliquity, λ, rather than the true 3D angle between the stellar rotation axis and the planetary orbital axis, ψ.[32] When the sky projection of the obliquity λ is combined with knowledge of the stellar inclination, $i_\star$, and the orbital inclination of the planet, the 3D obliquity ψ can be estimated. Recently, through constructing a sample of 3D obliquities, Albrecht et al. (2021) revealed a possible exoplanet architectural dichotomy, where hot Jupiters are primarily seen to orbit in either well-aligned orbits, or in close to polar orbits. However, the sample from Albrecht et al. (2021) is dominated by hot Jupiters—as such planets are the easiest to measure—and it is unclear if this reflects a property intrinsic to how hot Jupiters form, or if this dichotomy is more broadly seen for other types of planetary systems.

With the advent of next-generation RV spectrographs, we are capable of measuring the obliquities of smaller planets, and the growing sample of smaller planets with obliquity measurements hints that the dichotomy might also be seen for such planets (Stefansson et al. 2022). However, additional observations are needed to increase the size of the small sample ($\lesssim 10$). In this context, observations of low-mass planets ($\lesssim 0.3\,M_J$) in young systems (<1 Gyr) with precisely determined ages are particularly valuable, as they can help yield insights into the possible timescales involved in the different processes that are invoked to excite obliquities—such as planet–planet scattering (Rasio & Ford 1996), Von Zeipel–Lidov–Kozai oscillations (e.g., Fabrycky & Tremaine 2007; Naoz 2016), or secular resonance crossings with a dissapearing disk and a massive outer companion (Petrovich et al. 2020)—or dampen them through tidal interactions (see the discussion in Albrecht et al. 2012).

In this letter, we measure the stellar obliquity of TOI-2076 b, a warm sub-Neptune transiting a young (204 ± 50 MYr; Osborn et al. 2022) and active K-dwarf. The TOI-2076 planetary system—which hosts at least three transiting planets—was discovered by Hedges et al. (2021) using two sectors of photometric data from the Transiting Exoplanet Survey Satellite (TESS; Ricker et al. 2015). The system was further studied by Osborn et al. (2022) using the same two sectors in combination with data from the CHEOPS satellite (Benz et al. 2021), and revealed transit timing variations (TTVs) at the ~ 10 minute level. The known planets in the system have orbital periods of $P_b = 10.4$ days, $P_c = 21.0$ days, and $P_d = 35.1$ days, and radii of $R_b = 2.5\,R_\oplus$, $R_c = 3.5\,R_\oplus$, and $R_d = 3.2\,R_\oplus$, for planets b, c, and d, respectively (Osborn et al. 2022). Further, Zhang et al. (2022) recently claim evidence of He 10830 Å absorption during the transit of TOI-2076 b, suggesting that the atmosphere is experiencing atmospheric evaporation, though with additional observations Gaidos et al. (2022) caution that the absorption signature is most likely due to variability of the helium line due to stellar activity of the young star.

To constrain the obliquity of TOI-2076 b, we obtained spectroscopic in-transit observations using the NEID spectrograph (Halverson et al. 2016; Schwab et al. 2016) on the WIYN 3.5 m Telescope at the Kitt Peak National Observatory, which demonstrate that TOI-2076 b is in a well-aligned orbit. In addition, diffuser-assisted photometry using the engineered diffuser on the ARC 3.5 m Telescope at Apache Point Observatory (APO) reveal no flare events during transit that otherwise could complicate the RM analysis. TOI-2076 b joins a growing sample of warm Neptunes orbiting young stars in well-aligned orbits.

2. Observations

2.1. TESS

TESS (Ricker et al. 2015) observed TOI-2076 in three sectors: Sector 16 (2019 September 12 to October 6), Sector 23 (2020 March 19 to April 15), and Sector 50 (2022 March 26 to April 22) with the TESS two-minute cadence. TESS uses four CCD cameras to observe in the 600–1000 nm range, each with a $24° \times 24°$ field of view, resulting in a combined $24° \times 96°$ field of view. The TESS data were processed by the Science Processing Operations Center (SPOC; Jenkins et al. 2016) which removes systematic errors, and extracts the photometry. We retrieved the SPOC photometric data of TOI-2076 using the `lightkurve` (Lightkurve Collaboration et al. 2018) package. We analysed the Presearch Data Conditioning Single Aperture Photometry (PDCSAP) light curve, which contains systematics-corrected data using the algorithms originally developed for the Kepler data analysis pipeline. We removed 12,495 data points with TESS nonzero quality flags (e.g., due to guiding issues and excess stray light), leaving 38,950 data points for subsequent analysis.

2.2. NEID

We observed a transit of TOI-2076 b with the NEID spectrograph (Schwab et al. 2016) on the WIYN 3.5 m Telescope at Kitt Peak Observatory[33] on the night of 2022 February 13 for 5.5 hr. NEID is a high-resolution ($R \sim 113,000$) spectrograph covering a broad wavelength range from 380 to 930 nm. In total, using an exposure time of 600 s, we obtained 33 spectra spanning a period of 1 hr before and after the 3.3 hr transit (Hedges et al. 2021). The resulting median signal-to-noise ratio (S/N) was 105.1 at 5500 Å. The target rose from airmass 1.90 to 1.02 during the observation.

The NEID spectra were processed with the NEID Data Reduction Pipeline (DRP).[34] We extracted the RVs with a custom version of the Spectrum Radial Velocity Analyzer (SERVAL; Zechmeister et al. 2018) that we have adapted and optimized for NEID data (see Stefansson et al. 2022), using all of the available NEID spectra to generate a template for the RV calculation with SERVAL.[35] The resulting RVs agree well with the RVs from the NEID DRP derived with the cross-correlation function (CCF) method; the median RV error from the SERVAL pipeline is $0.88\,\mathrm{m\,s^{-1}}$ and it is $1.5\,\mathrm{m\,s^{-1}}$ from the

---

[32] In the special case where the differential rotation is known or can be measured the RM effect can place a constraint on the 3D obliquity (see, e.g., Gaudi & Winn 2007; Sasaki & Suto 2021).

[33] WIYN is a joint facility of the University of Wisconsin, Madison, Indiana University, the NSF's NOIRLab, the Pennsylvania State University, Purdue University, University of California, Irvine, and the University of Missouri.
[34] https://neid.ipac.caltech.edu/docs/NEID-DRP/
[35] We experimented creating a template derived only from spectra outside of the transit window. Doing so resulted in fully consistent RVs with only a $10\,\mathrm{cm\,s^{-1}}$ rms difference between the two different extractions.

CCF method. We elected to use the SERVAL RVs given their higher RV precision. The RV observations show a feature consistent with the RM effect as well as an upward RV trend that we explore in detail in Section 6.

2.3. Diffuser-assisted Photometry

During the spectroscopic transit, we obtained simultaneous photometry using the engineered diffuser (Stefansson et al. 2017) available on the Astrophysical Research Council Telescope Imaging Camera (ARCTIC) instrument (Huehnerhoff et al. 2016) on the ARC 3.5 m telescope at APO. To obtain high-precision observations of the bright star, we used the engineered diffuser, which spreads out the light of the star in a well-defined top-hat shape (Stefansson et al. 2017) while maintaining a stable point-spread function (PSF) throughout the observations. We observed the transit using the Sloan Digital Sky Survey (SDSS) i' filter with a short exposure time of 8 s due to the brightness of the host star. We used ARCTIC's 2×2 binning mode, resulting in a gain of 2.0 e/ADU and a plate scale of $0\farcs22$ pixel^{-1}. The target rose from airmass 1.72 to 1.01 during the observations. Wispy clouds during observation caused transparency fluctuations throughout the observations, which impacted the photometry.

To extract the photometry from the ARCTIC data, we used the AstroImageJ (Collins et al. 2017) software following the procedures in Stefansson et al. (2017), including bias and flat-field corrections. Prior to final aperture selection and analysis of the photometry, we used the astroscrappy (McCully et al. 2018) code to correct for cosmic rays and other charged particle events. We experimented with using a number of different apertures. For the final light curve analysed in this work, we used an aperture size of 25 pixels ($5\farcs5$) and sampled the background light with an annulus with an inner radius of 45 pixels ($9\farcs9$) and an outer radius of 65 pixels ($14\farcs3$) around the star as this resulted in the lowest rms errors. The six reference stars that resulted in the smallest error in the transit model were all substantially fainter than the target, by about 230 times on average. The observations show a transit-like feature consistent with the expected depth and duration of the transit at the expected time, and reveal no large flares during the transit, which otherwise could complicate the RM analysis.

3. Stellar Parameters

Table 1 shows the parameters of the host star TOI-2076 used in this work. We adopt the stellar rotation period from Hedges et al. (2021), $P_{\rm rot} = 7.27 \pm 0.23$ days, which is precisely determined using long-term ground-based photometry from the Kilodegree Extremely Little Telescope (KELT; Pepper et al. 2007). As an additional measurement of the stellar rotation period, we used the SpinSpotter (Holcomb et al. 2022) code—which uses the autocorrelation function (ACF) to measure stellar rotation periods. Using SpinSpotter on the three available TESS sectors, we obtain a stellar rotation period of $P_{\rm rot} = 7.251 \pm 0.073$ days. This value is consistent with the value in Hedges et al. (2021), although the uncertainty from SpinSpotter—which is estimated as the standard deviation of the spacing between ACF vertexes—is underestimated.

To constrain the stellar spectroscopic parameters, we used the SpecMatch-Emp[36] (Yee et al. 2017) code—which

Table 1
Summary of the Stellar Parameters Used in this Work

Parameter	Description	Value	Notes
d	Distance	41.963 ± 0.028 pc	(1)
$P_{\rm rot}$	Stellar rotation period	7.27 ± 0.23 days	(2)
Spectroscopic parameters from the NEID spectra:			
$T_{\rm eff}$	Effective temperature	5180 ± 110 K	(3)
[Fe/H]	Metallicity	-0.01 ± 0.09	(3)
R_*	Radius	$0.79 \pm 0.08\,R_\odot$	(3)
$v\sin i$	Projected rotational velocity	5 ± 1 km s^{-1}	(3)
Model-dependent stellar SED and isochrone fit parameters:			
M_*	Mass	$0.883 \pm 0.017\,M_\odot$	(3)
R_*	Radius	$0.772^{+0.015}_{-0.016}R_\odot$	(3)
ρ_*	Stellar density	2.720 ± 0.165 g cm^{-3}	(3)
$T_{\rm eff}$	Effective temperature	5201^{+66}_{-61} K	(3)
Age	Age	$0.338^{+0.077}_{-0.081}$ Gyr	(3)
[Fe/H]	Metallicity	$0.017^{+0.077}_{-0.056}$	(3)
$\log g$	Surface gravity in cgs units	4.608 ± 0.018	(3)

Note. References are: (1) Gaia (Gaia Collaboration 2021), (2) Hedges et al. (2021), and (3) This work.

constrains stellar spectroscopic parameters from comparing a spectrum of a star to a library of as-observed stars with well-constrained spectroscopic parameters—on the highest S/N NEID spectrum of TOI-2076 on segments of 100 Å between 5000 and 5800 Å. From the SpecMatch-Emp analysis, we obtained: $T_{\rm eff} = 5180 \pm 110$ K, [Fe/H] $= -0.01 \pm 0.09$, and $R_* = 0.79 \pm 0.08\,R_\odot$. To constrain the projected rotational velocity of the star, we used the SpecMatch-Synth[37] code (Petigura 2015), which compares the spectrum of a star to a library of theoretical spectra (Coelho et al. 2005) that can be artificially broadened to obtain estimates of $v\sin i$. In doing so, we obtained $v\sin i = 5 \pm 1$ km s^{-1} for TOI-2076. The uncertainties from these codes were internally calibrated using a "leave-one-out" procedure with the empirical library of well-characterized stars and observed spectra, and the uncertainties were found to be robust even at S/Ns as low as 20 per 1D extracted pixel. To obtain a model-dependent constraint on the mass and radius of the star, we performed a spectral energy distribution (SED) fit using the SpecMatch-Emp values and other available magnitudes and priors available from the literature using the EXOFASTv2 code (Eastman et al. 2019) leveraging the Yonsei–Yale stellar isochrone models. The final values are summarized in Table 1.

4. Photometric Analysis

To constrain the orbital ephemerides of TOI-2076 b precisely—important for the RM effect modeling—we utilized the juliet code (Espinoza et al. 2019) to perform a fit of the available TESS and diffuser-assisted APO transit photometry. As TTVs have been reported in the system with $\sim$10–15 minute amplitudes (Osborn et al. 2022; Zhang et al. 2022), we leveraged the functionality within juliet to account for TTVs by fitting the individual transit midpoints of the TESS transits and the APO transits separately. Our derived transit midpoints for TOI-2076 b are within 1σ with those reported in Osborn et al. (2022) and Zhang et al. (2022). For the fit, we used the dynesty dynamic nested sampler

---

[36] https://github.com/samuelyeewl/specmatch-emp

[37] https://github.com/petigura/specmatch-syn

Table 2
Summary of the Priors and Resulting Posteriors for the Photometric Analysis

Parameter	Description	Priors	Posteriors
`juliet` input parameters:			
T_{TESS_0} (BJD$_{\text{TDB}}$)	Transit midpoint, 1st transit	$\mathcal{N}(2458743.7248, 0.042)$	$2458743.7183^{+0.0045}_{-0.0054}$
T_{TESS_1}	Transit midpoint, 2nd transit	$\mathcal{N}(2458754.080049, 0.042)$	$2458754.0768^{+0.0022}_{-0.0026}$
$T_{\text{TESS}_{19}}$	Transit midpoint, 20th transit	$\mathcal{N}(2458940.474531, 0.042)$	$2458940.4810^{+0.0097}_{-0.0020}$
$T_{\text{TESS}_{20}}$	Transit midpoint, 21st transit	$\mathcal{N}(2458950.82978, 0.042)$	$2458950.8343^{+0.0097}_{-0.0020}$
$T_{\text{TESS}_{89}}$	Transit midpoint, 90th transit	$\mathcal{N}(2459665.341961, 0.042)$	$2459665.3542^{+0.0038}_{-0.0052}$
$T_{\text{TESS}_{90}}$	Transit midpoint, 91st transit	$\mathcal{N}(2459675.69721, 0.042)$	$2459675.6942^{+0.0019}_{-0.0018}$
$T_{\text{TESS}_{91}}$	Transit midpoint, 92nd transit	$\mathcal{N}(2459686.052459, 0.042)$	$2459686.0510^{+0.0014}_{-0.0013}$
$T_{\text{APO}_{85}}$	Transit midpoint, 86th transit	$\mathcal{N}(2459623.920965, 0.042)$	$2459623.9183^{+0.0011}_{-0.0016}$
R_p/R_*	Radius ratio	$\mathcal{U}(0.0, 0.1)$	$0.0284^{+0.0011}_{-0.0010}$
e	Eccentricity	0.0	0.0
ω	Argument of periastron (°)	90.0	90.0
b	Impact parameter	$\mathcal{U}(0.0, 1.0)$	$0.123^{+0.077}_{-0.073}$
ρ	Stellar density (cgs)	$\mathcal{N}(2.720, 0.165)$	$2.712^{+0.099}_{-0.110}$
$q_{1\text{TESS}}$	Linear limb darkening parameter	$\mathcal{U}(0.0, 1.0)$	$0.724^{+0.186}_{-0.230}$
$q_{2\text{TESS}}$	Quadratic limb darkening parameter	$\mathcal{U}(0.0, 1.0)$	$0.463^{+0.227}_{-0.192}$
$M_{\text{Dilution,TESS}}$	Dilution factor	1.0	1.0
$M_{\text{Flux,TESS}}$	Offset relative flux	$\mathcal{N}(0.0, 0.1)$	$-0.001^{+0.001}_{-0.001}$
$\sigma_{W\text{TESS}}$	Jitter (ppm)	$\mathcal{J}(1.0, 5000.0)$	$140.7^{+5.1}_{-5.1}$
$q_{1\text{APO}}$	Linear limb darkening parameter	$\mathcal{U}(0.0, 1.0)$	$0.196^{+0.170}_{-0.119}$
$q_{2\text{APO}}$	Quadratic limb darkening parameter	$\mathcal{U}(0.0, 1.0)$	$0.602^{+0.256}_{-0.322}$
$M_{\text{Dilution,APO}}$	Dilution factor	1.0	1.0
$M_{\text{Flux,APO}}$	Offset relative flux	$\mathcal{U}(0.0, 0.1)$	$0.00246^{+0.00026}_{-0.00024}$
$\sigma_{W\text{APO}}$	Jitter (ppm)	$\mathcal{J}(1.0, 5000.0)$	$999.30^{+0.51}_{-1.02}$
Detrending parameters:			
B_{TESS}	GP amplitude	$\mathcal{J}(10^{-6}, 1.0)$	$0.000019^{+0.000008}_{-0.000005}$
C_{TESS}	GP additive factor	$\mathcal{J}(0.001, 1000.0)$	$0.014^{+0.058}_{-0.011}$
L_{TESS}	GP length scale (days)	$\mathcal{J}(0.0, 100000.0)$	$11.99^{+5.19}_{-3.10}$
P_{TESS}	GP period (days)	$\mathcal{J}(2.0, 10.0)$	$4.01^{+0.17}_{-0.16}$[a]
$\theta_{0\text{APO}}$	Linear regressor coefficient (APO airmass)	$\mathcal{U}(-100.0, 100.0)$	$0.002^{+0.002}_{-0.002}$
Derived parameters:			
T_C (BJD$_{\text{TDB}}$)	Transit midpoint	⋯	$2458743.7247^{+0.0027}_{-0.0022}$
P	Orbital period (days)	⋯	$10.35527^{+0.00003}_{-0.00004}$
a/R_*	Scaled semimajor axis	⋯	$24.87^{+0.30}_{-0.33}$
i	Inclination (°)	⋯	$89.72^{+0.17}_{-0.18}$
S_{flux}	Insolation flux ($S_\oplus$)	⋯	$49.4^{+2.9}_{-2.7}$
T_{14}	Full transit duration (days)	⋯	$0.1352^{+0.0016}_{-0.0018}$
T_{23}	Interior transit duration (days)	⋯	$0.1275^{+0.0016}_{-0.0017}$
τ	Ingress time (days)	⋯	$0.0038^{+0.00017}_{-0.00016}$
R_p	Planetary radius ($R_\oplus$)	⋯	$2.39^{+0.10}_{-0.10}$
$T_{\text{eq},a=0}$	Planet equilibrium temperature, albedo $a = 0$ (K)[b]	⋯	738.0 ± 10.0

Notes. $\mathcal{N}(m, \sigma)$ denotes a normal prior with mean m and standard deviation σ; $\mathcal{U}(a, b)$ denotes a uniform prior with start value a and end value b; and $J(a, b)$ denotes a log-uniform distribution between lower limit a and upper limit b.
[a] This value is not equal to the stellar rotation period value, which is $7.27 \pm .23$ days as reported in Table 1. See the discussion in Section 4.
[b] Calculated assuming the whole surface is the emitting area.

(Speagle 2020) to sample the posteriors and the `batman` package (Kreidberg 2015) to generate the light-curve models. The priors and posteriors from the fit are summarized in Table 2. Figure 1 shows the TESS photometry along with the best-fit model and the phase-folded TESS photometry after accounting for the TTVs. The APO photometry and the best-fit model are shown in Figure 2.

To remove clear correlated noise signatures seen in the TESS data, we used the "quasi-periodic" Gaussian Process kernel from the `celerite` package (Foreman-Mackey et al. 2017) available in `juliet`. Broad uninformative priors were placed on the Gaussian process (GP) hyper parameters. We note that

the GP value $P_{\text{TESS}} = 4.01^{+0.17}_{-0.16}$ in Table 2 is different than our adopted value for the stellar rotation period of 7.27 ± 0.23 days listed in Table 1. We attribute this difference being due to a combination of data gaps, and different spot evolution/behavior seen in the different TESS sectors. The latter two TESS sectors show faster timescale variability than the first TESS sector, which we attribute to the young and active star likely having developed more spot complexes at different latitudes/longitudes. As noted in Section 1, we adopt the 7.27 ± 0.23 days value as the rotation period, as that value is derived from eight years of ground-based monitoring as discussed in Hedges et al. (2021).
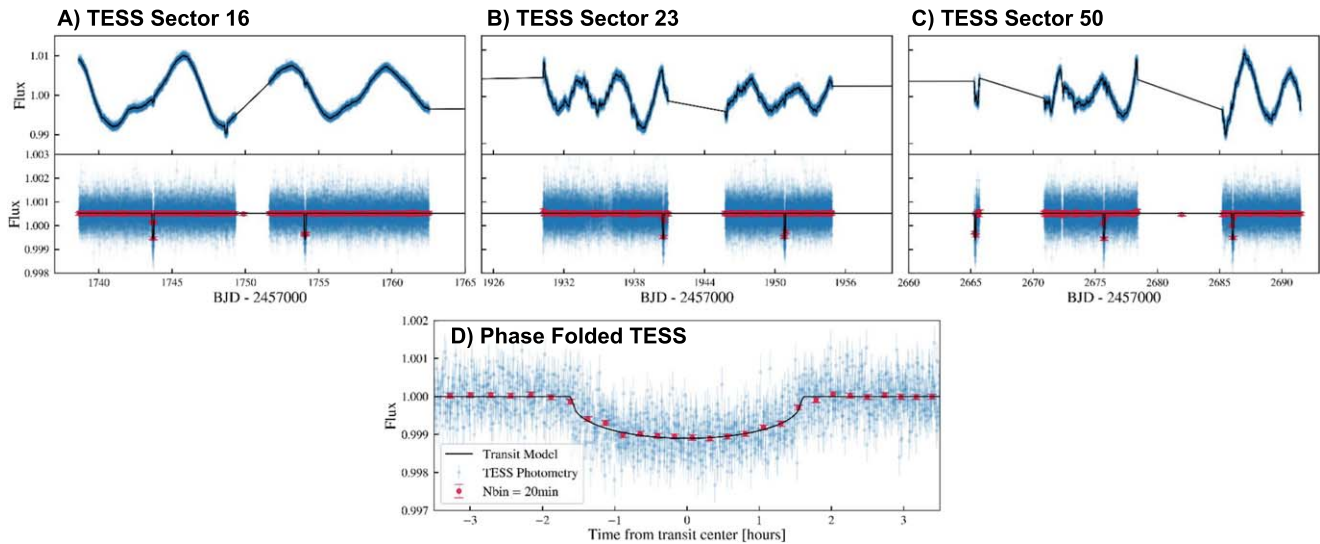
Figure 1. TESS lightcurves of TOI-2076 from (A) Sector 16, (B) Sector 23, and (C) Sector 50. The top row shows the TESS photometry (blue points) with along with a transit model for TOI-2076 b + GP model (red) to account for stellar activity. The middle panel shows the photometry after subtracting the quasi-periodic GP model, revealing the TOI-2076 b transits. Panel (D) shows the phase-folded TESS photometry phased to the orbital period of TOI-2076 b, with the transit model overlaid.

For the ground-based APO data, we observed a smooth trend during the observations. To remove the trend, we employed the linear detrending models available in `juliet`. We experimented detrending with a number of linear detrending parameters, including the airmass, x, and y centroid coordinates, time, etc. We found that a linear detrending using the airmass parameter yielded the highest quality fit measured from the residual scatter in the photometry after subtracting the detrended transit model from the data.

For the fit, we placed an informative Gaussian prior on the stellar density of $2.720 \pm 0.165 \, \mathrm{g \, cm^{-3}}$ (see Table 1). We used the (q_1, q_2) limb darkening parameterization as described in Kipping (2013). We experimented with a circular and an eccentric fit to model the photometry. Given that we only see a minimal statistical preference of $\Delta \ln(Z) = 0.42$ in favor of the eccentric model and that the posteriors between the two runs were within 1σ of each other (the eccentric model yielded a coarse constraint on $e = 0.28^{+0.37}_{-0.23}$ with $e < 0.77$ at 95% confidence), we elected to model the photometry assuming a circular orbit. This agrees with the approach of Hedges et al. (2021). Given the large $a/R_\star \sim 25$ for TOI-2076 b, we acknowledge that it is a possibility that additional precise photometric observations could constrain the eccentricity further.

5. RM Effect

To model the RM effect, we used the `rmfit` package (see Stefansson et al. 2022), which implements the RM effect model from Hirano et al. (2011b). For the model, we placed informative priors on the transit parameters (P, T_C, $R_p/R_\star$, i, $a/R_\star$) as constrained by the photometric analysis in Section 4. We placed informative priors on the limb darkening parameters u_1 and u_2. To arrive at a self-consistent constraint on the 3D obliquity ψ, in the RM model, we follow the RM parameterization discussed in Stefansson et al. (2022), who parameterizes the RM model in terms of the sky-projected obliquity λ, stellar inclination ($\cos i_\star$), stellar rotation period (P_{rot}), and stellar radius ($R_\star$) as variables in the Markov Chain Monte Carlo (MCMC) sampling. $v \sin i_\star$ is then estimated as

$v \sin i_\star = v\sqrt{1 - \cos^2 i_\star}$, where we estimate the equatorial velocity as $v_{\mathrm{eq}} = v = 2\pi R_\star/P_{\mathrm{rot}}$.[38] We then estimate the obliquity using,

$$\cos(\psi) = \sin(i_\star)\cos(\lambda)\sin(i) + \cos(i_\star)\cos(i), \quad (1)$$

where i is the orbital inclination of the planet. For the final MCMC fit, we ran 100 walkers using the `emcee` package (Foreman-Mackey et al. 2013) for 30,000 steps after removing 2000 steps as burn-in steps. To determine that the chains were converged, we leveraged a few methods. First, we verified that the Gelman–Rubin (GR) statistic was within $\ll 1\%$ of unity. However, the GR statistic has limitations in assessing convergence, especially when the walkers are not independent (see, e.g., the discussion in Hogg & Foreman-Mackey 2018), so in addition to the GR statistic, we follow the suggestion in Hogg & Foreman-Mackey (2018) and estimated the autocorrelation length of our chains, where the mean autocorrelation length was $\tau_{\mathrm{mean}} = 202$, and the maximum autocorrelation length was $\tau_{\mathrm{max}} = 261$. From running 30,000 steps, this ensures that each chain has at least 100 independent samples, which is more than the chain length of $50\,\tau$ as suggested in the `emcee` documentation.[39] From these lines of evidence combined with visual inspection of the chains suggesting convergence, we conclude the chains are well mixed.

To account for the RV trend seen during the observations, we simultaneously fit the RM effect with an RV slope. We also experimented with adding a quadratic curvature to the slope. However, doing so did not significantly improve the resulting fit where the difference in the Bayesian information criterion was ΔBIC $= 3.0$ in favor of the quadratic model, suggesting only a modest statistical preference for the more complicated model, where both models yielded the same constraints on the

---

[38] This broadly follows the methodology in Masuda & Winn (2020) to account for the fact that $v \sin i_\star$ and v_{eq} are not independent variables. As we are assuming solid body rotation, the equatorial velocity equals the rotational velocity of the star.

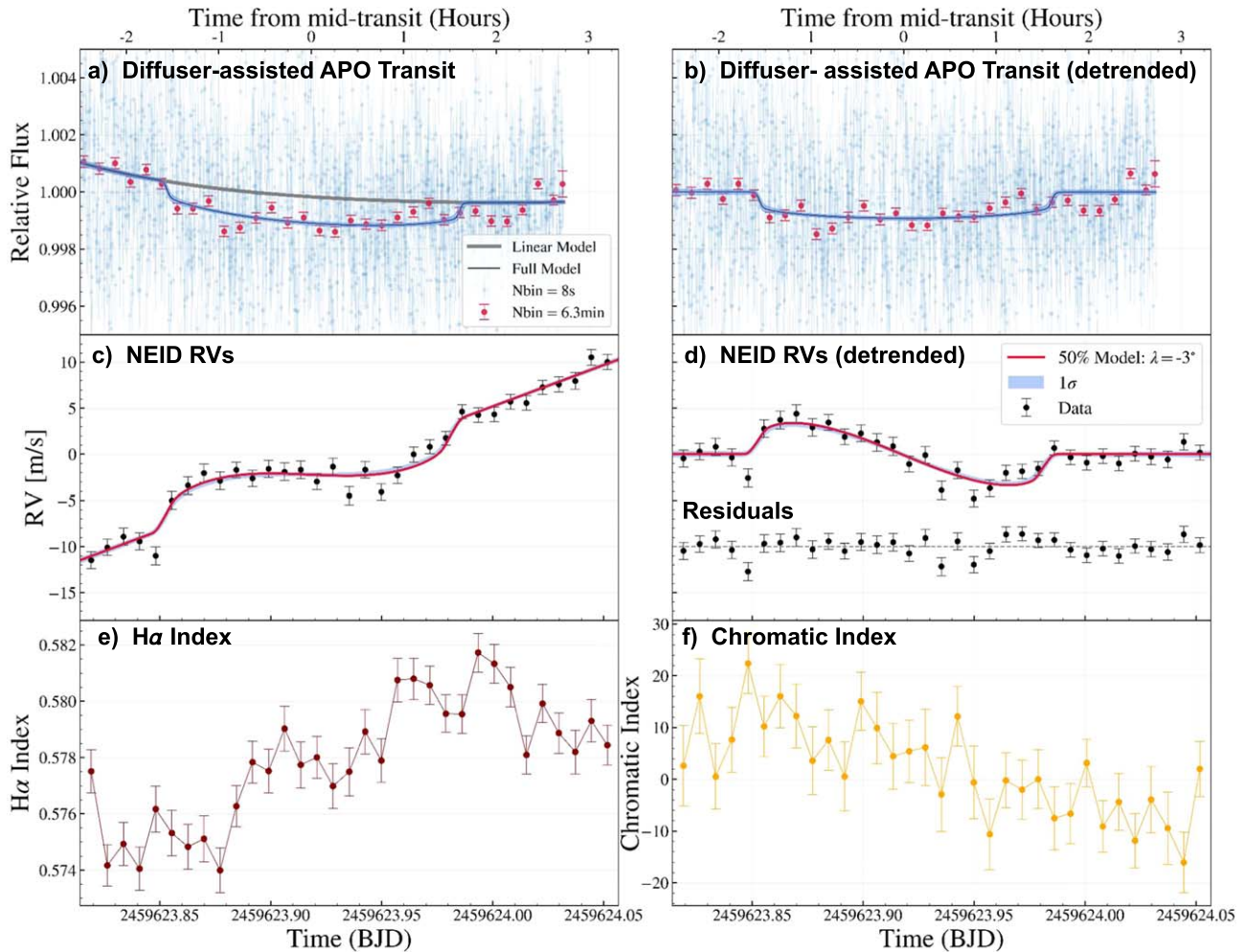[39] See notes here: https://emcee.readthedocs.io/en/latest/tutorials/autocorr/#autocorr

Figure 2. (a) Diffuser-assisted photometry from APO with the transit model from the joint APO and TESS fit overlaid in blue. The linear model of the airmass is shown in gray. (b) Diffuser-assisted photometry and the joint transit model detrended from the linear model of the airmass. (c) NEID RV data during the transit of TOI-2076 b revealing a clear detection of the RM effect. We attribute the positive slope to stellar activity. (d) NEID RV data detrended from the overall upward slope and the corresponding residuals. (e) Hα index from NEID RV observations. (f) CRX from the NEID RV observations. The data are available as data-behind the figure.

(The data used to create this figure are available.)

key parameters of interest of $v \sin i_\star$ and λ. Given the low statistical preference, we adopted the simpler linear model. As the semi-amplitude of the planet K—which is currently unconstrained as TOI-2076 b does not have a measured mass —is degenerate with the linear RV slope during the short observing baseline, we elected to fix the semi-amplitude of the planet to zero and let the slope parameter fully account for the long-term RV trend during the observations. Table 3 summarizes the input priors and the best-fit posterior values.

Figure 2 shows a plot of the data along with the best-fit RM effect model. Our best-fit model suggests a sky-projected velocity of $v \sin i = 5.27^{+0.24}_{-0.29}$ km s^{-1}, a sky-projected obliquity of $\lambda = -3^{+16}_{-15}$ °, and a obliquity of $\psi = 18^{+10}_{-9}$ ° ($\psi < 34°$ at 95% confidence). The $v \sin i_\star$ value agrees with $v \sin i_\star = 5 \pm 1$ km s^{-1} from the spectral-broadening measurements in Table 1. The obliquity value of $\psi = 18^{+10}_{-9}$ ° suggests that TOI-2076 b is in a well-aligned orbit.

As an additional test, we fit the RM effect using the more conventional parameterization of λ and $v \sin i$ placing uniform priors on $v \sin i_\star$ from 0 to 10 km s^{-1}, instead of the $\cos i_\star$, $R_\star$, and $P_{\rm rot}$ parameterization discussed above. In doing so, we

obtain a λ of -3^{+13}_{-14} ° and $v \sin i_\star = 5.28^{+0.23}_{-0.28}$ km s^{-1}, which agree with the values above. We elect to use the former parameterization to arrive at a self-consistent constraint of the obliquity, ψ.

6. Discussion

6.1. Impact of Stellar Activity on the RM Analysis

TOI-2076 shows clears signatures of stellar activity due to its young age of 204 ± 50 MYr. The TESS data show photometric variations with an amplitude of $\sim 1\%$ (Figure 1). Additionally, Figure 2 shows a clear trend in the RVs during the RM observations with an amplitude of ~ 20 m s^{-1} across the full 5.5 hr observing baseline. This trend is in the opposite direction to what we would expect due to the planet-induced stellar RV, which we estimated to have an RV semi-amplitude of $K = 2.0^{+1.5}_{-0.8}$ m s^{-1} (assuming a predicted mass of $6.3^{+4.5}_{-2.6} M_\oplus$ using the mass–radius relation from the Forecaster package; Chen & Kipping 2017). Such inverse trends have been previously reported in RM observations of other young systems: Wirth et al. (2021) observed an RV trend of

Table 3
Summary of the Priors and Resulting Posteriors for the RM Analysis

Parameter	Description	Prior	Posterior
MCMC input parameters:			
T_C (BJD$_{\mathrm{TDB}}$)	Transit midpoint	$\mathcal{N}(2458743.7247, 0.0025)$	2458743.7219 ± 0.0019
P	Orbital period (days)	$\mathcal{N}(10.35527, 0.00003)$	10.355235 ± 0.00002
R_p/R_*	Radius ratio	$\mathcal{N}(0.0284, 0.0011)$	0.02881 ± 0.00095
a/R_*	Scaled semimajor axis	$\mathcal{N}(24.87, 0.31)$	25.07 ± 0.28
i	Transit inclination (°)	$\mathcal{N}(89.72, 0.18)$	89.65 ± 0.17
e	Eccentricity	0.	0
ω	Argument of periastron (°)	90.	90.
K	RV semi-amplitude (m s^{-1})	0	0
γ	NEID RV offset (m s^{-1})	$\mathcal{U}(-50, 50)$	-0.59 ± 0.18
u_1	Linear limb darkening parameter	$\mathcal{N}(0.35, 0.1)$	$0.416_{\pm}0.098$
u_2	Quadratic limb darkening parameter	$\mathcal{N}(0.32, 0.1)$	0.332 ± 0.050
β	Intrinsic stellar line width (km s^{-1})	$\mathcal{N}(6.0, 1.0)$	5.4 ± 1.0
λ	Sky-projected obliquity (deg)	$\mathcal{U}(-180, 180)$	-3_{-15}^{+16}
$R_\star$	Radius of star ($R_\odot$)	$\mathcal{N}(0.772, 0.015)$	0.774 ± 0.015
P_{rot}	Stellar rotation period (days)	$\mathcal{N}(7.27, 0.23)$	7.21 ± 0.22
$\cos i_\star$	Cosine of stellar inclination	$\mathcal{U}(0, 1)$	$0.2_{-0.14}^{+0.18}$
$\dot{\gamma}$	Slope of RVs (m s^{-1} day^{-1})	$\mathcal{U}(-500, 500)$	89.7 ± 2.4
Derived parameters:			
$v \sin i_\star$	Projected rotational velocity (km s^{-1})	…	$5.27_{-0.22}^{+0.24}$
$i_\star$	Stellar inclination (deg)	…	79_{-11}^{+8}
ψ	Obliquity (deg)	…	18_{-9}^{+10}

Note. $\mathcal{N}(m, \sigma)$ denotes a normal prior with mean m and standard deviation σ and $\mathcal{U}(a, b)$ denotes a uniform prior with start value a and end value b.
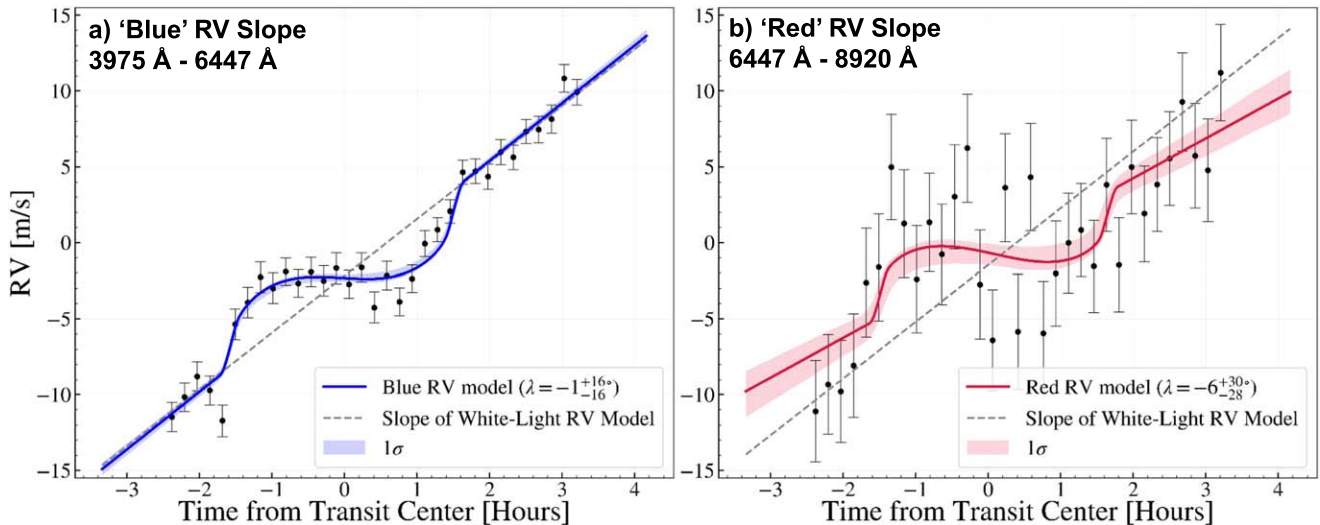
Figure 3. Comparing the RM fit to "blue-only" RVs (a) and "red-only" RVs (b). The RV curve for the "blue-only" RV orders spans orders from 3975–6447 Å and the "red-only" orders span orders from 6447–8920 Å. For comparison, the slope of the "white-light" RV model used in the full analysis is overplotted as the gray-dashed line in both panels. The slope in the blue orders is steeper than in the red, suggesting the RV slope is due to stellar activity such as a spot on the surface of the star.

$\sim$75 m s^{-1} over a similar baseline ($\sim$19 m s^{-1} hr^{-1}) in RM observations of the 60 Myr old TOI-942b, and Benatti et al. (2019) observed an even larger RV trend of $\sim$150 m s^{-1} ($\sim$25 m s^{-1} hr^{-1}) for the 45 Myr old DS Tuc A b.

In addition to the photometry and the RVs, Figure 2 also shows the Hα index along with the chromatic index (CRX), both of which show slow trends during the RM observations. We calculated both indices following the definition in Zechmeister et al. (2018). The Hα index is particularly sensitive to flares (e.g., Ichimoto & Kurokawa 1984), and the lack of flare-like features and/or high-frequency variations suggests that no large flares occurred during the observations,

consistent with the photometric observations. CRX is defined in Zechmeister et al. (2018) as the best-fit straight-line slope fitted to order-by-order RVs as a function of wavelength, which is measured as the velocity per unit wavelength ratio. A nonzero CRX value signifies that a trend is seen in the order-by-order RVs as a function of wavelength, a strong indication of stellar activity. From the CRX values shown in Figure 2(f), we see indications of a chromaticity in the RVs. To examine this behavior further, we split the RV data in two groups of "blue" orders (3975–6447 Å) and "red" orders (6447–8920 Å), as seen in Figure 3. Separate RV fits to these "blue" and "red"
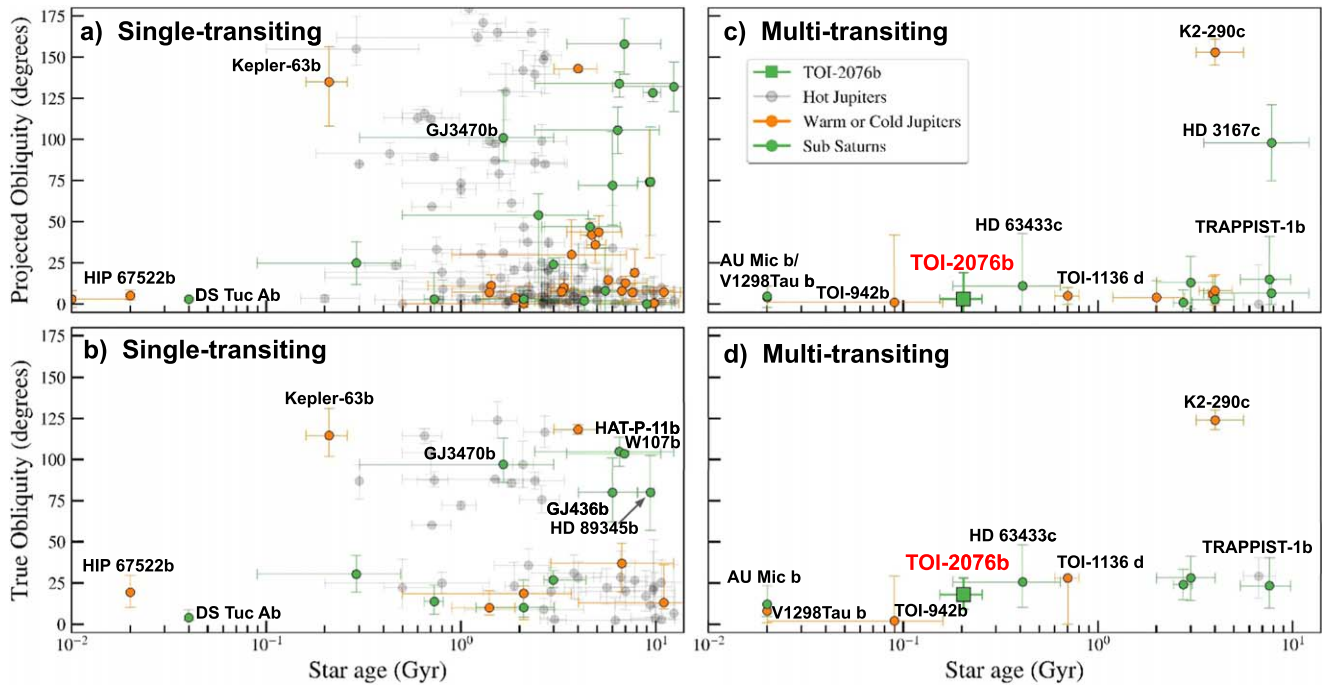
Figure 4. Sky-projected obliquities (a, c) and 3D obliquities (b, d) for planetary systems as a function of age for single-transiting (a, b), and multi-transiting (c, d) systems. Planets with masses $>0.3\,M_J$ and $a/R_\star < 10$ are classified as hot Jupiters (black points), and as warm Jupiters if $a/R_\star > 10$ (orange points). Planets with masses $<0.3\,M_J$ are classified as sub-Saturns regardless of the value of $a/R_\star$. This classification system is adopted from Albrecht et al. (2022). Despite a lack of a mass measurement of TOI-2076 b we classify it as a sub-Saturn due to its radius and distance. The position of TOI-2076 b is highlighted in red. Obliquity measurements for systems excluding TOI-2076 are drawn from Albrecht et al. (2022), Dai et al. (2023), Bourrier et al. (2023), and the TEPCAT database (Southworth 2011) where the error in the sky-projected obliquity was $\Delta\lambda < 40°$, and the fractional error on the age of the system was less than 90%. W107b denotes WASP-107b.

extractions resulted in RV slopes of $\dot{\gamma}_{\rm blue} = 91.3^{+2.4}_{-2.5}\,{\rm m\,s^{-1}\,day^{-1}}$, and $\dot{\gamma}_{\rm red} = 62.9 \pm 8.5\,{\rm m\,s^{-1}\,day^{-1}}$, respectively. The shallower slope value seen at the red wavelengths is expected if the activity signature is due to a starspot with a differing contrast as a function of wavelength compared to the stellar photosphere, further confirming that the slope is due to activity. Best-fit RM models to the "blue" and "red" RV extractions returned $v\sin i$, λ, and ψ values consistent with the values ("white-light") reported in Table 3, suggesting that our treatment of a simple line to remove the RV trend is sufficient to remove the activity signature and does not impact the determination of the obliquity.

To estimate further the expected RV impact of a possible starspot moving on the stellar surface during the RM observations, we used the SOAP2.0 code (Dumusque et al. 2014). For the starspot simulation, we assumed a stellar inclination of $i_\star = 80°$, consistent with the median value from our RM analysis. We experimented by placing different spots of different sizes and found that placing two circular spots with a temperature contrast of $\Delta 500\,{\rm K}$ of radius $0.23\,R_\star$ (covering 2.6% of the visible hemisphere) at latitudes of $30°$ resulted in $\sim$1% photometric variations peak-to-valley, consistent with the amplitude of variations seen in the TESS photometry. The expected peak-to-valley RV variations from such spots was $\sim$150 m s^{-1}, which would cause an $\sim$19 m s^{-1} RV variation during the 5.5 hr observing baseline. This is in good agreement with the RV trend we see in Figure 2(c). We note that this is not a unique solution, as due to degeneracies between different spot parameters, including spot size, latitude, and contrast, there is a good possibility that different spot configurations could also explain the observed photometry. However, as a configuration

exists that is compatible with the TESS photometry and the NEID RVs, we conclude that the observed RV slope is likely due to stellar activity.

6.2. Obliquities as a Function of Age

TOI-2076 b joins a small but growing group of planets in young systems with multiple transiting planets with measured obliquities. Figure 4 compares the obliquity of TOI-2076 b to obliquity measurements of other known exoplanets in single and multi-transiting planet systems as a function of the age of the system.

For systems with a single transiting planet, we see that highly misaligned planets are only seen for ages $\gtrsim$200 Myr, where the Kepler-63b system—hosting a Saturn-size planet in a 9.4 day orbit around a young 210 MYr Sun-like star—is the youngest system hosting a highly misaligned planet with $\lambda = -135^{+21.2}_{-26.8}$ and $\psi = 114.6^{+16.6}_{-12.5}$ (Sanchis-Ojeda et al. 2013; Bourrier et al. 2023). For older systems ($\gtrsim$1 Gyr), there is a growing population of eccentric sub-Saturns that are on misaligned orbits, including WASP-107b (Rubenzahl et al. 2021), GJ 436 b (Bourrier et al. 2018, 2022), GJ 3470b (Stefansson et al. 2022), HD 89345b (Bourrier et al. 2023), and HAT-P-11b (Hirano et al. 2011a; Winn et al. 2010). Three of these systems—WASP-107b, GJ 3470b, and HAT-P-11b—have known outer companions or candidate outer companions that have been suggested as possible paths to explain the misalignments of the inner transiting planets via gravitational interactions. However, the story is not fully clear, as the GJ 436 b system does not have a known outer companion in the system, and there are some sub-Saturns in eccentric orbits that are observed to be in well-aligned orbits (e.g., K2-25b; Stefansson et al. 2020). This could possibly indicate that

different formation mechanisms are at play. The fact that misaligned planets with high obliquities are only seen around systems with ages $\gtrsim 200$ Myr, potentially points to that the origin of misalignment might not be primordial and is rather caused by dynamical interactions later on. However, the mechanisms that are often invoked to explain misalignments —secular resonance crossings due to a disappearing disk and a massive outer companion (Petrovich et al. 2020), and Von Zeipel–Kozai–Lidov oscillations (Fabrycky & Tremaine 2007; Naoz 2016)—occur on relatively fast timescales of 10^5–10^6 yr, so the lack of misalignments of the youngest small planets continues to be noteworthy. Additional obliquity constraints of the very youngest systems (<100 MYr) will be particularly valuable.

For the systems with multiple transiting planets (multi-transiting systems), we see from Figure 4 that there are no known young multi-transiting systems with ages $\lesssim 1$–3 Gyr on misaligned orbits. We see that there are two older misaligned multi-transiting systems: K2-290 (Hjorth et al. 2021) and HD 3167c (Dalal et al. 2019), with ages $\gtrsim 3$ GYr. Interestingly, these systems have contrasting architectures: K2-290 hosts two planets, K2-290 b and c in coplanar orbits, whereas HD 3167 b and c have mutual inclinations of $\sim 90°$ (Bourrier et al. 2021). To explain the misalignments, for the K2-290 system it has been suggested that the outer star K2-290 B (projected separation of 110 au) could have tilted the protoplanetary disk of K2-290 A, causing K2-290 b and c to form coplanar in an initially misaligned disk (Hjorth et al. 2021). An alternative formation scenario was suggested by Best & Petrovich (2022), in which the third star in the triple system, K2-290 C (projected separation of 2500 au), could be responsible for the misalignment of both planets through gravitational perturbations at much longer timescales (typically $\gtrsim 100$ Myr). For the HD 3167 system, Bourrier et al. (2021) suggest that the perpendicular architecture likely arose from the outer planet being tilted through gravitational interactions with a possible outer companion, while the inner ultrashort period planet likely retained a low obliquity due to tight tidal-coupling with the host star.

In contrast to the misaligned multi-planet systems, for TOI-2076 b there are multiple lines of evidence suggesting that TOI-2076 b formed via a more dynamically benign process of smooth disk migration in an initially well-aligned disk. First, the large $a/R_\star \sim 25$ value for TOI-2076 b makes tidal realignment inefficient, making TOI-2076 b a pristine probe of the initial formation angle. This, combined with the currently observed low obliquity of TOI-2076 b, disfavors a scenario where TOI-2076 b experienced a high degree of misalignment that was subsequently realigned. Second, the planets in the TOI-2076 system orbit close to period commensurabilities (b and c at close to 2:1 resonance; c and d close to 5:3 resonance) with clear TTVs observed in the system (Osborn et al. 2022), which demonstrate that the planets in the TOI-2076 system are tightly gravitationally interacting. Therefore, an appealing formation scenario for the compact TOI-2076 b system is through smooth disk migration within an initially well-aligned protoplanetary disk (e.g., Goldreich & Tremaine 1979, 1980), where the planets migrated into their resonant orbits that we see today. Future RM effect observations of TOI-2076 c and d will help constrain the coplanarity of the system, which through these lines of evidence we would expect to be likely well-aligned with the orbit of planet b. TOI-2076 b is similar to the recently studied TOI-1136 system (Dai et al. 2023), which is a compact network of at least six transiting planets in a resonant chain that likely formed through smooth disk migration in an initially well-aligned disk.

7. Summary

Using high-precision in-transit spectroscopic observations with the NEID spectrograph on the WIYN 3.5 m Telescope at Kitt Peak Observatory, we determined that the young (204 ± 50 Myr) sub-Neptune planet TOI-2076 b has a low sky-projected obliquity of $\lambda = -3^{+16}_{-15}°$. Leveraging knowledge of the size of the star and the stellar rotation period, we estimate an obliquity of $\psi = 18^{+10}_{-9}°$ and a stellar inclination of $i_\star = 79^{+8}_{-11}°$, suggesting that TOI-2076 b is in an orbit well-aligned with the stellar equator of its host star. Three sectors of data from TESS along with precise diffuser-assisted photometry from ARCTIC on the ARC 3.5 m telescope at APO were used to constrain the orbital parameters of the planet precisely.

TOI-2076 b joins a small, but growing sample of young multi-planet systems on well-aligned orbits. It is the fourth planet with an age $\leqslant 300$ Myr in a multi-transiting system with an obliquity measurement. The well-aligned orbit of TOI-2076 b together with the compact multi-planet configuration that shows evidence of TTVs suggests that the TOI-2076 system likely formed via convergent disk migration in an initially well-aligned disk. This would suggest that TOI-2076 c and d are likely coplanar to TOI-2076 b. Additional RM observations of the outer planets are needed to confirm this hypothesis.

In addition, due to its brightness, TOI-2076 hosts some of the most accessible young planets for atmospheric characterization. With a measurement of its obliquity, the architecture of the TOI-2076 system is now better understood, which will help place any future follow-up observations—such as atmospheric characterization—in further context.

ORCID iDs

Robert C. Frazier ⓘ https://orcid.org/0000-0001-6569-3731
Gudmundur Stefánsson ⓘ https://orcid.org/0000-0001-7409-5688
Suvrath Mahadevan ⓘ https://orcid.org/0000-0001-9596-7983
Samuel W. Yee ⓘ https://orcid.org/0000-0001-7961-3907
Caleb I. Cañas ⓘ https://orcid.org/0000-0003-4835-0619
Joshua N. Winn ⓘ https://orcid.org/0000-0002-4265-047X
Jacob Luhn ⓘ https://orcid.org/0000-0002-4927-9925
Fei Dai ⓘ https://orcid.org/0000-0002-8958-0683
Lauren Doyle ⓘ https://orcid.org/0000-0002-9365-2555
Heather Cegla ⓘ https://orcid.org/0000-0001-8934-7315
Shubham Kanodia ⓘ https://orcid.org/0000-0001-8401-4300
Paul Robertson ⓘ https://orcid.org/0000-0003-0149-9678
John Wisniewski ⓘ https://orcid.org/0000-0001-9209-1808
Chad F. Bender ⓘ https://orcid.org/0000-0003-4384-7220
Jiayin Dong ⓘ https://orcid.org/0000-0002-3610-6953
Arvind F. Gupta ⓘ https://orcid.org/0000-0002-5463-9980
Samuel Halverson ⓘ https://orcid.org/0000-0003-1312-9391
Suzanne Hawley ⓘ https://orcid.org/0000-0002-6629-4182
Leslie Hebb ⓘ https://orcid.org/0000-0003-1263-8637
Rae Holcomb ⓘ https://orcid.org/0000-0002-5034-9476
Adam Kowalski ⓘ https://orcid.org/0000-0001-7458-1176
Jessica Libby-Roberts ⓘ https://orcid.org/0000-0002-2990-7613
Andrea S. J. Lin ⓘ https://orcid.org/0000-0002-9082-6337
Michael W. McElwain ⓘ https://orcid.org/0000-0003-0241-8956
Joe P. Ninan ⓘ https://orcid.org/0000-0001-8720-5612
Cristobal Petrovich ⓘ https://orcid.org/0000-0003-0412-9314
Arpita Roy ⓘ https://orcid.org/0000-0001-8127-5775
Christian Schwab ⓘ https://orcid.org/0000-0002-0091-7105
Ryan C. Terrien ⓘ https://orcid.org/0000-0002-4788-8858
Jason T. Wright ⓘ https://orcid.org/0000-0001-6160-5888

References

Albrecht, S., Winn, J. N., Johnson, J. A., et al. 2012, ApJ, 757, 18
Albrecht, S. H., Dawson, R. I., & Winn, J. N. 2022, PASP, 134, 082001
Albrecht, S. H., Marcussen, M. L., Winn, J. N., Dawson, R. I., & Knudstrup, E. 2021, ApJL, 916, L1
Astropy Collaboration, Robitaille, T. P., Tollerud, E. J., et al. 2013, A&A, 558, A33
Benatti, S., Nardiello, D., Malavolta, L., et al. 2019, A&A, 630, A81
Benz, W., Broeg, C., Fortier, A., et al. 2021, ExA, 51, 109
Best, S., & Petrovich, C. 2022, ApJL, 925, L5
Bourrier, V., Lovis, C., Cretignier, M., et al. 2021, A&A, 654, A152
Bourrier, V., Lovis, C., Beust, H., et al. 2018, Natur, 553, 477
Bourrier, V., Zapatero Osorio, M. R., Allart, R., et al. 2022, A&A, 663, A160
Bourrier, V., Attia, O., Mallonn, M., et al. 2023, A&A, 669, A63
Chen, J., & Kipping, D. 2017, ApJ, 834, 17

Coelho, P., Barbuy, B., Melendez, J., Schiavon, R. P., & Castilho, B. V. 2005, A&A, 443, 735

Collins, K. A., Kielkopf, J. F., Stassun, K. G., & Hessman, F. V. 2017, AJ, 153, 77

Dai, F., Masuda, K., Beard, C., et al. 2023, AJ, 165, 33

Dalal, S., Hébrard, G., Lecavelier des Étangs, A., et al. 2019, A&A, 631, A28

Dumusque, X., Boisse, I., & Santos, N. C. 2014, ApJ, 796, 132

Eastman, J. D., Rodriguez, J. E., Agol, E., et al. 2019, arXiv:1907.09480

Espinoza, N., Kossakowski, D., & Brahm, R. 2019, MNRAS, 490, 2262

Fabrycky, D., & Tremaine, S. 2007, ApJ, 669, 1298

Foreman-Mackey, D. 2016, JOSS, 1, 24

Foreman-Mackey, D., Agol, E., Ambikasaran, S., & Angus, R. 2017, AJ, 154, 220

Foreman-Mackey, D., Hogg, D. W., Lang, D., & Goodman, J. 2013, PASP, 125, 306

Fulton, B. J., Petigura, E. A., Blunt, S., & Sinukoff, E. 2018, PASP, 130, 044504

Gaia Collaboration, Brown, A. G. A., Vallenari, A, et al. 2021, A&A, 649, A1

Gaidos, E., Hirano, T., Lee, R. A., et al. 2023, MNRAS, 518, 3777

Gaudi, B. S., & Winn, J. N. 2007, ApJ, 655, 550

Ginsburg, A., Sipocz, B., Parikh, M., et al. 2018, astropy/astroquery v0.3.7 release, Zenodo, doi:10.5281/zenodo.1160627

Goldreich, P., & Tremaine, S. 1979, ApJ, 233, 857

Goldreich, P., & Tremaine, S. 1980, ApJ, 241, 425

Halverson, S., Terrien, R., Mahadevan, S., et al. 2016, Proc. SPIE, 9908, 99086P

Hedges, C., Hughes, A., Zhou, G., et al. 2021, AJ, 162, 54

Hirano, T., Narita, N., Shporer, A., et al. 2011a, PASJ, 63, 531

Hirano, T., Suto, Y., Winn, J. N., et al. 2011b, ApJ, 742, 69

Hjorth, M., Albrecht, S., Hirano, T., et al. 2021, PNAS, 118, e2017418118

Hogg, D. W., & Foreman-Mackey, D. 2018, ApJS, 236, 11

Holcomb, R. J., Robertson, P., Hartigan, P., Oelkers, R. J., & Robinson, C. 2022, ApJ, 936, 138

Huehnerhoff, J., Ketzeback, W., Bradley, A., et al. 2016, Proc. SPIE, 9908, 99085H

Hunter, J. D. 2007, CSE, 9, 90

Ichimoto, K., & Kurokawa, H. 1984, SoPh, 93, 105

Jenkins, J. M., Twicken, J. D., McCauliff, S., et al. 2016, Proc. SPIE, 9913, 99133E

Kanodia, S., & Wright, J. 2018, RNAAS, 2, 4

Kluyver, T., Ragan-Kelley, B., Pérez, F., et al. 2016, in Positioning and Power in Academic Publishing: Players, Agents and Agendas, ed. F. Loizides & B. Scmidt (Amsterdam: IOS Press), 87

Kipping, D. M. 2013, MNRAS, 435, 2152

Kreidberg, L. 2015, PASP, 127, 1161

Lightkurve Collaboration, Cardoso, J. V. d., Hedges, C., et al. 2018, Lightkurve: Kepler and TESS time series analysis in Python, Astrophysics Source Code Library, ascl:1812.013

Masuda, K., & Winn, J. N. 2020, AJ, 159, 81

McCully, C., Crawford, S., Kovacs, G., et al. 2018, Astropy/Astroscrappy v1.0.5, Zenodo, doi:10.5281/zenodo.1482019

McKinney, W. 2010, in Proc. 9th Python in Science Conf., ed. S. van der Walt & J. Millman (Austin, TX: SciPy), 51

McLaughlin, D. B. 1924, ApJ, 60, 22

Morris, B. M., Tollerud, E., Sipocz, B., et al. 2018, AJ, 155, 128

Naoz, S. 2016, ARA&A, 54, 441

Osborn, H. P., Bonfanti, A., Gandolfi, D., et al. 2022, A&A, 664, A156

Parviainen, H. 2016, PyDE v1.5, Zenodo, doi:10.5281/zenodo.45602

Pepper, J., Pogge, R. W., DePoy, D. L., et al. 2007, PASP, 119, 923

Petigura, E. 2015, arXiv:1510.03902

Petrovich, C., Munoz, D. J., Kratter, K. M., & Malhotra, R. 2020, ApJL, 902, L5

Rasio, F. A., & Ford, E. B. 1996, Sci, 274, 954

Ricker, G. R., Winn, J. N., Vanderspek, R., et al. 2015, JATIS, 1, 014003

Rossiter, R. A. 1924, ApJ, 60, 15

Rubenzahl, R. A., Dai, F., Howard, A. W., et al. 2021, AJ, 161, 119

Sanchis-Ojeda, R., Winn, J. N., Marcy, G. W., et al. 2013, ApJ, 775, 54

Sasaki, S., & Suto, Y. 2021, PASJ, 73, 1656

Schwab, C., Rakich, A., Gong, Q., et al. 2016, Proc. SPIE, 9908, 99087H

Southworth, J. 2011, MNRAS, 417, 2166

Speagle, J. S. 2020, MNRAS, 493, 3132

Stefansson, G., Mahadevan, S., Hebb, L., et al. 2017, ApJ, 848, 9

Stefansson, G., Mahadevan, S., Wisniewski, J., et al. 2018, Proc. SPIE, 10702, 1070250

Stefansson, G., Mahadevan, S., Maney, M., et al. 2020, AJ, 160, 192

Stefansson, G., Mahadevan, S., Petrovich, C., et al. 2022, ApJL, 931, L15

Van Der Walt, S., Colbert, S. C., & Varoquaux, G. 2011, CSE, 13, 22

Winn, J. N., Johnson, J. A., Howard, A. W., et al. 2010, ApJL, 723, L223

Wirth, C. P., Zhou, G., Quinn, S. N., et al. 2021, ApJL, 917, L34

Yee, S. W., Petigura, E. A., & von Braun, K. 2017, ApJ, 836, 77

Zechmeister, M., Reiners, A., Amado, P. J., et al. 2018, A&A, 609, A12

Zhang, M., Knutson, H. A., Dai, F., et al. 2023, AJ, 165, 62